

Vision-Based 3-D Control of Magnetically Actuated Catheter Using BigMag—An Array of Mobile Electromagnetic Coils

Jakub Sikorski , *Student Member, IEEE*, Alper Denasi , *Member, IEEE*, Giuseppe Bucchi, Stefano Scheggi , and Sarthak Misra , *Member, IEEE*

Abstract—Automated steering of endovascular catheters has a potential of improving the outcome of minimally invasive surgical procedures. Nevertheless, actuation, tracking, and closed-loop position control of catheters remain a challenge. In this study, we present a modular framework for a three-dimensional (3-D) position control of magnetically actuated endovascular catheter. The catheter is fitted with a permanent magnet and deflected using externally generated magnetic field provided by BigMag—An array of mobile electromagnets. Pseudorigid-body modeling is used to formulate an inverse-model closed-loop position controller of the catheter. The shape feedback is reconstructed from a 3-D point cloud of catheter silhouette, obtained using stereo vision. Magnetic actuation is enabled using an inverse field map technique, mapping the reference magnetic field to BigMag configuration variables. The framework is tested in a series of experiments. The inverse map is validated, showing a mean magnetic field error of 2.20%. The accuracy of the shape reconstruction algorithm is 0.59 mm. Finally, the magnetically actuated catheter is steered across a series of trajectories with maximum reported catheter deflection of 68.43° and maximum tip speed of 5 mm/s. Across all trajectories, the best control performance metrics are the mean error of 0.57 mm and the RMS error of 0.77 mm.

Index Terms—Magnetic devices, Medical robotics, motion control, robot sensing systems.

Manuscript received February 21, 2018; revised August 19, 2018; accepted December 31, 2018. Date of publication January 16, 2019; date of current version April 16, 2019. Recommended by Technical Editor X. Chen. This work was supported by the European Research Council through the European Union's Horizon 2020 Research and Innovation programme under Grant Agreement #638428 - project ROBOTAR. (*Corresponding author: Jakub Sikorski.*)

J. Sikorski, G. Bucchi, and S. Scheggi are with the Surgical Robotics Laboratory, Department of Biomechanical Engineering, University of Twente, Enschede 7500 AE, The Netherlands (e-mail: j.sikorski@utwente.nl; g.bucchi@utwente.nl; s.scheggi@utwente.nl).

A. Denasi and S. Misra are with the Surgical Robotics Laboratory, Department of Biomechanical Engineering, University of Twente, Enschede 7500 AE, The Netherlands and also with the Department of Biomedical Engineering, University of Groningen, 9702 CP, The Netherlands and University Medical Centre Groningen, 9713 GZ, The Netherlands (e-mail: a.denasi@utwente.nl; s.misra@utwente.nl).

This paper has supplementary downloadable material available at <http://ieeexplore.ieee.org>, provided by the author.

Color versions of one or more of the figures in this paper are available online at <http://ieeexplore.ieee.org>.

Digital Object Identifier 10.1109/TMECH.2019.2893166

I. INTRODUCTION

ENDOASCULAR catheters are an important class of surgical devices used for minimally invasive surgery (MIS) within the human cardiovascular system [1]. These catheters are inserted through small incisions in limbs and navigated through blood vessels to reach more centrally located target sites, such as the brain or the heart. Conventional MIS navigation of endovascular catheters is manual, which significantly limits its precision, thus requiring skilled personnel in order to ensure patient safety. By employing robotic technology, steering of endovascular catheters can be facilitated. This has already been demonstrated in several standard MIS procedures [2], [3].

Steerable catheters can become versatile tools, capable of reaching any desired target within the cardiovascular system. Nevertheless, ensuring reliable actuation and control of such devices still poses a significant challenge. From the perspective of robotics, catheters are classified as continuum manipulators (CMs), that is, manipulators having a hyperredundant structure of continuously bending elastic elements. In most applications, CMs are actuated using tendons or guide-wires, and modeled as arcs with constant curvature [4]–[6]. Due to the small size of the catheters and their nonhomogeneous structural compositions, limitations of this solution are pronounced. The accuracy of tendon steering is limited due to actuation hysteresis and inaccuracies of constant curvature approximation. Furthermore, significant friction experienced by the tendons can lead to their failure, threatening the safety of the patient [7].

The first suggestion that magnetic interaction can be used to remotely steer CM was postulated over 60 years ago [8]. Magnetic CM can be made safer, and smaller than the ones driven by tendons, due to their simpler structure involving no moving parts. Therefore, this actuation technique is well-suited for endovascular catheters.

Magnetically actuated catheters presented in the literature can be broadly divided into passive or active devices [9]. Active magnetic catheters are fitted with microcoils, which generate variable magnetic dipole moments. If located in a large static external magnetic field of a magnetic resonance scanner (MRS), such catheters can be deflected by controlling the electric currents flowing through microcoils [10], [11]. On the contrary, the passive catheters are fitted with permanent magnets with constant magnetic dipole moments, and steered by varying the

external magnetic field generated by custom, dedicated systems [12], [13].

Evaluating both classes of devices from a practical point of view, passive magnetic catheters are better suited for automated endovascular procedures. If the dipole provided by a microcoil is aligned with the field of MRS, the catheter loses a degree of freedom (DoF) [14]. Moreover, the microcoils are expensive and difficult to manufacture, and their heat dissipation causes safety concerns [15]. Passive catheters display none of these limitations. They can be readily assembled using inexpensive and accessible elements. Furthermore, they allow for 5 DoF actuation irrespective of their pose within the workspace.

Magnetic guidance systems employing passive catheters are already available commercially, yet they rely entirely on open-loop control performed by the surgeon [16]. Catheter steering using closed-loop position control has so far received limited attention. A two-dimensional (2-D) steering has been approached in several studies, using linear control with decoupling [17]–[19]. Nevertheless, none of these techniques were extended to 3-D position control.

The first successful attempt thereat has been presented recently in [20]. This technique employs a 3-D nonlinear position controller, based on the geometrically exact Cosserat rod model. However, this approach has been demonstrated only for small angle deflections and slow effective motion speed of the catheter tip. This is due to limitations caused by the low bandwidth of the magnetic actuation system used, inadequate shape feedback, and computational complexity of the rod model.

The closed-loop steering of the CM is enabled by feedback providing the information about the shape of the device in real-time. Medical imaging modalities, such as fluoroscopy or ultrasound, are preferred for that purpose since they are capable of providing information in reference to tissues inside the body. Imaging data is usually available in the form of 3-D point clouds. Several techniques to reconstruct the shape of a CM from 3-D point clouds have already been presented. However, their limitations, such as low computational performance or inability to track CM undergoing larger bends, suggest the need for an alternative [21], [22].

In this paper, we present a modular framework for modeling, tracking, and control of passive magnetic catheters. The passive magnetic catheters (Fig. 1) is represented using a computationally efficient pseudorigid-body model (PRBM). We employ the elements of two existing quasi-static models based on this approach to derive an analytical (i.e., computationally fast) formulation of manipulator Jacobian [14], [23]. Consequently, our PRBM is used to derive a nonlinear inverse model controller for steering of a magnetic catheter tip in a 3-D space. The proposed controller uses the shape feedback from a 3-D point-cloud, processed using a novel reconstruction technique. This technique offers a very good computational performance, being in the same time suitable for processing point-clouds from various imaging modalities.

The catheter is actuated using BigMag, an array of mobile electromagnetic coils, which offers magnetic actuation in a large workspace with high bandwidth [24]. In this paper, we extend on our previous work, presenting how to employ BigMag for

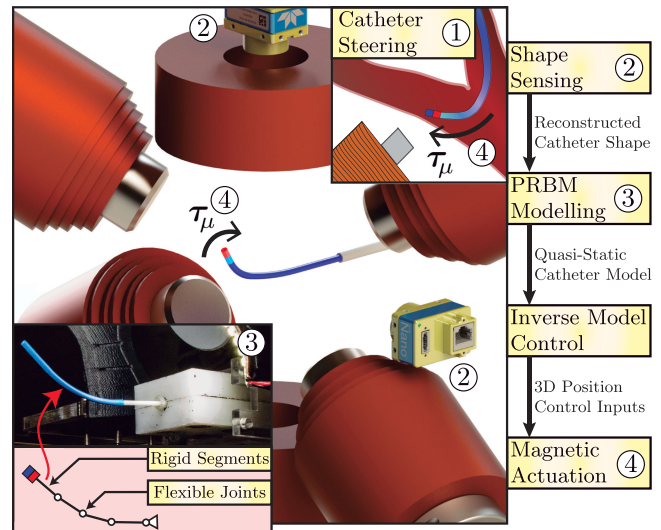


Fig. 1. ① In this integrative study, we present a framework for 3-D position control of magnetically actuated catheter. ② An iterative algorithm tracks the shape of the catheter using 3-D point clouds provided by stereo vision system. ③ The reconstructed shape is approximated by PRBM. ④ We use PRBM to formulate an inverse model controller for 3-D position control of the catheter employing magnetic torques (τ_μ). The torques are generated using BigMag—an array of mobile coils.

accurate actuation of magnetic catheter. To the authors' best knowledge, BigMag is the first array of mobile coils used for that purpose.

The rest of this paper is structured as follows. In Section II, we present a PRBM of a passive magnetic catheter. Section III presents an inverse map method, which allows the use of the BigMag system for magnetic actuation. The shape reconstruction algorithm is given in Section IV. The full control framework is presented in Section V. Finally, Section VI details the experiments and discusses the results, validating our steering technique, and Section VII summarizes this paper and gives recommendations for further studies.

II. MODELING A MAGNETIC CATHETER

Magnetic catheter exhibits highly nonlinear dynamical behavior. The modeling of this behavior is impractical for high bandwidth position control. Therefore, we propose to approximate catheter mechanics with a computationally fast, quasi-static PRBM. This model describes the shape of the catheter under the influence of an external magnetic torque and gravity forces. Moreover, it provides an analytical formulation of body manipulator Jacobian, and thus, can be effectively applied in real-time for catheter steering.

Let us start by considering the shape of a magnetic catheter (see Fig. 2), which can be described by a continuous, smooth function ($\mathbf{P}(s) : \Omega_p \mapsto \Omega_w$), such that

$$\Omega_p = \{s \in \mathbb{R} \mid 0 \leq s \leq l\} \quad (1)$$

$$\Omega_w = \{x, y, z \in \mathbb{R} \mid \underline{x} \leq x \leq \bar{x}, \underline{y} \leq y \leq \bar{y}, \underline{z} \leq z \leq \bar{z}\} \quad (2)$$

where \star and $\bar{\star}$ are the limits of the workspace for $\star = \{x, y, z\}$. In (1), the parameter (s) defines the position along the length

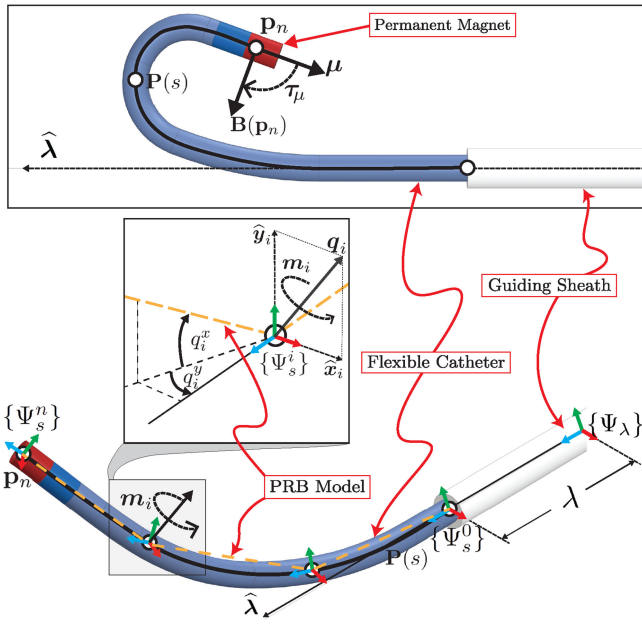


Fig. 2. Top: Magnetic catheter has a single magnet at its tip, represented by magnetic dipole moment (μ). In presence of external magnetic field ($\mathbf{B}(\mathbf{p}_n)$), the catheter is bending due to magnetic torque (τ_μ). Its shape can be represented by a 3-D curve ($\mathbf{P}(s)$) Bottom: The kinematics of bending flexible catheter can be approximated using a quasi-static PRBM. The manipulator is represented with a series of discrete rigid segments ($i \in [1; n]$) connected by 2 DoF elastic joints. Each elastic joint (i) is affected by the corresponding joint torque ($\mathbf{m}_i \in \mathbb{R}^3$). The deflection due to that torque is parametrized by a set of two angles (q_i^x, q_i^y).

of the catheter, spanning between base point ($s = 0$) and the tip ($s = l$). Consequently, $l \in \mathbb{R}^+$ is the total length of the catheter and Ω_w is its workspace defined as a subset of Cartesian space.

The magnetic catheter is connected to a guiding sheath (see Fig. 2) used for insertion. The stiffness of the sheath is much higher than the one of the catheter; therefore, we neglect its role in the bending of the catheter. Using PRB discretization technique, we can represent the flexible catheter by (n) rigid segments. The segments are described by reference frames ($\{\Psi_s^i\}$, $i = 1, \dots, n$), each located at a point ($\mathbf{p}_i = \mathbf{P}(i \frac{l}{n}) \in \mathbb{R}^3$). Additionally, frame $\{\Psi_s^0\}$ located at \mathbf{p}_0 denotes the base of the catheter.

The catheter is assumed to be an externally loaded incompressible beam. The torsion and buckling of the catheter are neglected. The shape ($\mathbf{P}(s)$) of the catheter is determined by a mechanical load applied along its length, which follows from Euler–Bernoulli beam theory. We approximate this total load by a point wrench ($\mathbf{W} \in \mathbb{R}^6$), acting at the tip of the catheter ($\mathbf{p}_n = \mathbf{P}(l) \in \mathbb{R}^3$). \mathbf{W} is defined in body reference frame and comprises of a magnetic force ($\mathbf{F}_\mu \in \mathbb{R}^3$) and a magnetic torque ($\tau_\mu \in \mathbb{R}^3$). Both \mathbf{F}_μ and τ_μ are exerted on the catheter due to the interaction of the dipole moment ($\mu \in \mathbb{R}^3$) located at the catheter tip (\mathbf{p}_n) with the external magnetic field ($\mathbf{B}(\mathbf{p}_n) \in \mathbb{R}^3$) as follows:

$$\mathbf{W} = \begin{bmatrix} \mathbf{F}_\mu \\ \tau_\mu \end{bmatrix} = \begin{bmatrix} \nabla(\mu^T \mathbf{B}(\mathbf{p}_n)) \\ S(\mu) \mathbf{B}(\mathbf{p}_n) \end{bmatrix} \quad (3)$$

where $S(\alpha)$ for any vector (α) indicates its skew-symmetric representation. We assume the catheter to be in a reference configuration when $\mathbf{W} = \mathbf{0}_{6 \times 1}$. Given the insertion axis ($\hat{\lambda} \in \mathbb{R}^3$) passing through the base of the catheter ($\mathbf{p}_0 = \mathbf{P}(0) \in \mathbb{R}^3$), the shape of the manipulator at the reference configuration is a straight line ($\mathbf{P}(s) = s\hat{\lambda}$).

In PRBM approximation, the rigid segments representing the catheter are connected in series by a total of n 2DoF flexible, revolute joints (Fig. 2). The total rotation of joint i is expressed with respect to frame ($\{\Psi_s^{i-1}\}$) as $\mathbf{q}_i = \mathbf{w}_i^x q_i^x + \mathbf{w}_i^y q_i^y \in \mathbb{R}^3$, where $q_{i,x}, q_{i,y} \in \mathbb{S}$ are joint variables, $\mathbf{w}_i^x, \mathbf{w}_i^y \in \mathbb{R}^3$ are instantaneous joint axes derived as in [14]. Collecting the joint variables, we define the total manipulator configuration as follows:

$$\mathbf{q} = [q_{1,x} \quad q_{1,y} \quad \dots \quad q_{n,x} \quad q_{n,y}]^T \in \mathbb{R}^{2n}. \quad (4)$$

The pose of each frame ($\{\Psi_s^i\}$) with respect to ($\{\Psi_s^0\}$) is represented by a homogeneous transformation (${}^0\mathbf{H}(\mathbf{q}) = \begin{bmatrix} \mathbf{R}_i(\mathbf{q}) & \mathbf{p}_i(\mathbf{q}) \\ \mathbf{0}_{1 \times 3} & 1 \end{bmatrix} \in \text{SE}(3)$). Furthermore, if we define a twist associated with each joint (i) as follows:

$$\hat{\xi}_i = \begin{bmatrix} S(\mathbf{q}_i) S(\mathbf{p}_{i-1}(\mathbf{0})) \mathbf{q}_i \\ \mathbf{0}_{1 \times 3} & 0 \end{bmatrix} \in \text{se}(3) \quad (5)$$

the transformation (${}^j\mathbf{H}(\mathbf{q}) \in \text{SE}(3)$, $j = 0, \dots, i-1$) between any two frames ($\{\Psi_s^j\}$) and ($\{\Psi_s^i\}$) can be calculated from the following product of exponentials:

$${}^j\mathbf{H}(\mathbf{q}) = e^{\hat{\xi}_{j+1}} \dots e^{\hat{\xi}_i} {}^j\mathbf{H}(\mathbf{0}). \quad (6)$$

The PRBM technique represents the internal compliance of the flexible catheter using torsional springs located at each joint (i). Due to this compliance, the particular configuration (\mathbf{q}) of a catheter depends on the effect of tip wrench on PRBM joints (see Fig. 2). This effect is represented by joint torques ($\mathbf{m} \in \mathbb{R}^{2n}$). Hence, the joint-space equation of motion of the catheter takes the following form:

$$\mathbf{m} = \mathbf{C}\mathbf{q} + \mathbf{Z}(\mathbf{q})\dot{\mathbf{q}} + \mathbf{g}(\mathbf{q}) \quad (7)$$

where $\mathbf{C} \in \mathbb{R}^{2n \times 2n}$ is a positive-definite diagonal compliance matrix, $\mathbf{Z}(\mathbf{q}) \in \mathbb{R}^{2n \times 2n}$ is the positive-semidefinite viscous damping matrix, and $\mathbf{g}(\mathbf{q}) \in \mathbb{R}^{2n}$ is the vector of moments due to gravity. The entries of \mathbf{C} represent the PRBM torsional spring constants, and depend on the flexural rigidity of the catheter as shown in our previous work [23].

Using the principle of virtual work, the body manipulator Jacobian ($\mathbf{J}_b(\mathbf{q}) \in \mathbb{R}^{6 \times 2n}$) is used to relate tip wrench (\mathbf{W}), defined as in (3), and the joint torques (\mathbf{m}). We calculate $\mathbf{J}_b(\mathbf{q})$ using the derivation proposed by Greigarn and Çavuşoğlu [14]. The final model of the catheter is developed by combining (3) and (7). The gravity is modeled by a point load ($\mathbf{F}_g \in \mathbb{R}^3$) located at the tip (\mathbf{p}_n) of the catheter. We consider it to be the force due to the weight of the dipole (which has a much higher mass than the flexible tubing). Hence, the final static equilibrium equation is as follows:

$$\mathbf{J}_b^T(\mathbf{q})\mathbf{W} = \mathbf{C}\mathbf{q} - \mathbf{J}_b^T \begin{bmatrix} \mathbf{R}_n^T(\mathbf{q})\mathbf{F}_g \\ \mathbf{0}_{3 \times 1} \end{bmatrix}. \quad (8)$$

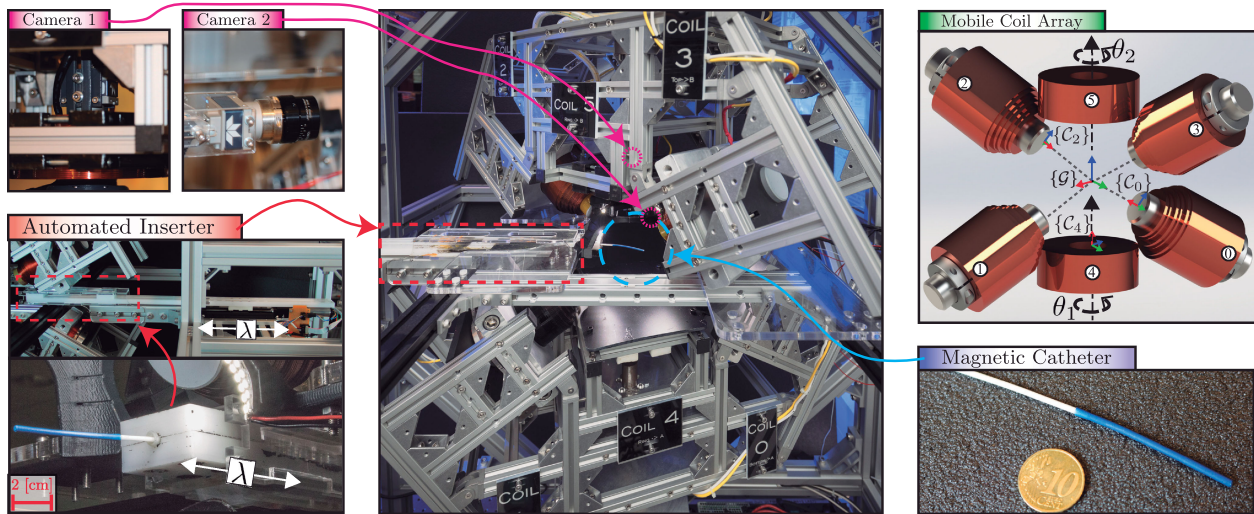


Fig. 3. BigMag is an array of six mobile coils, capable of providing actuation of magnetic catheters in a spherical workspace with a diameter of 10 cm (blue circle). Moreover, BigMag is equipped with an automated inserter (red rectangle) controlling the insertion position of the magnetic catheter (λ), and two cameras used for stereo vision. The coils of BigMag are located on two independently rotating fixtures around the Z axis of global reference frame ($\{G\}$). Each coil (k) generates magnetic field expressed in a local reference frame ($\{C_k\}$). The position of fixture holding coils (0, 1, 4) is described by angle (θ_1), whereas θ_2 denotes the position of fixture for coils (2, 3, 5). The axes in all reference frames are red, green, and blue for X , Y , and Z , respectively.

Note that we neglect the weight of the catheter tubing, as it is an order of magnitude lower than F_g . Moreover, the effect of the viscous damping ($Z(\mathbf{q})$) is disregarded, due to the quasi-static assumption.

Driving the catheter to the static equilibrium described by (8), requires an external system capable of precise generation of prescribed magnetic wrenches (\mathbf{W}). Usually, magnetic forces (\mathbf{F}_μ) with magnitudes sufficient for catheter steering are unachievable in large workspace due to rapid decay of magnetic field gradients at a distance from the field source [17]. Consequently, \mathbf{F}_μ is neglected in our study, and thus, the torques ($\boldsymbol{\tau}_\mu$) are selected as the sole control inputs for catheter steering. As follows from (3), these torques arise due to magnetic field ($\mathbf{B}(\mathbf{p}_n)$) at the position of the catheter tip (\mathbf{p}_n). Therefore, a reliable method of generating such a field for any point inside the workspace must be made available for catheter steering. The following section presents our solution.

III. MODELING OF BIGMAG COIL ARRAY

The system used in this study for tracking and control of magnetic catheters is called BigMag (see Fig. 3). It is an array of six mobile electromagnetic coils placed in two mobile fixtures, capable of rotating around a spherical workspace with a diameter of 10 cm. The design of the system has already been introduced in details in our previous study [24]. This section presents an updated inverse map technique, which relates the desired magnetic field ($\mathbf{B}(\mathbf{p}_n)$) to the set of BigMag configuration variables: coil currents ($\boldsymbol{\mathcal{I}} = [I_0 \cdots I_5] \in \mathbb{R}^6$) and coil fixture positions ($\theta_1, \theta_2 \in \mathbb{S}$).

The technique is derived in a few steps. First, the forward map of the array is introduced, describing $\mathbf{B}(\mathbf{p}_n)$ for a given configuration of BigMag. Due to rotating coils, the forward map is highly nonlinear, hence its analytical inversion is challenging. However, the overactuation of BigMag allows reformulating the

inverse map as an optimization problem minimizing power consumption of the array. We analyze the behavior of this problem in simulation to propose an inverse map, which provides the desired solution taking into account the limits on coil currents and on fixture velocities.

A. Forward Map of BigMag Coil Array

In our model, a unit component of the array is a single coil, referred to with an index ($k \in [0, 5]$). The coil has fixed dimensions and material composition. For every coil (k), we construct a local reference frame ($\{C_k\}$) coincident with the long axis of the coil (see Fig. 3). The position of point (\mathbf{p}_n) expressed in reference frame ($\{C_k\}$) is described by vector ($\mathbf{p}_n^{C_k} \in \mathbb{R}^3$). The coil is assumed to operate in its linear region. Thus, the magnetic field ($\mathbf{B}_{C_k} \in \mathbb{R}^3$) at $\mathbf{p}_n^{C_k}$ depends linearly on coil current ($I_k \in \mathbb{R}$) and is given as follows:

$$\mathbf{B}_{C_k}(\mathbf{p}_n^{C_k}) = I_k \boldsymbol{\beta}_k^{C_k}(\mathbf{p}_n^{C_k}) \quad (9)$$

where $\boldsymbol{\beta}_k^{C_k}(\mathbf{p}_n^{C_k}) \in \mathbb{R}^3$ is the unit field map of coil (k) at $\mathbf{p}_n^{C_k}$ [24]. In this study, we develop $\boldsymbol{\beta}_k^{C_k}(\mathbf{p}_n^{C_k})$ using a measurement-based, axisymmetric representation similar to [25].

The forward model of BigMag is constructed assuming the magnetic fields generated by each coil (k) of BigMag follow the principle of superposition, providing the total field (\mathbf{B}_G). This field is expressed in the global reference frame ($\{G\}$) located in the center of BigMag workspace (see Fig. 3). The field map ($\boldsymbol{\beta}^{C_k}(\mathbf{p}_n^{C_k})$) is used to describe the effect of each coil on the total field. Since for each coil, the map is expressed in local reference frame ($\{C_k\}$), we develop a coordinate transformation to express $\boldsymbol{\beta}^{C_k}(\mathbf{p}_n^{C_k})$ in global reference frame.

Let us start by defining variables describing the kinematics of BigMag. The rotation matrix (${}^G_{C_k} \mathbf{R} \in \text{SO}(3)$), describes the orientation of frame ($\{C_k\}$) for coil (k) as a function of

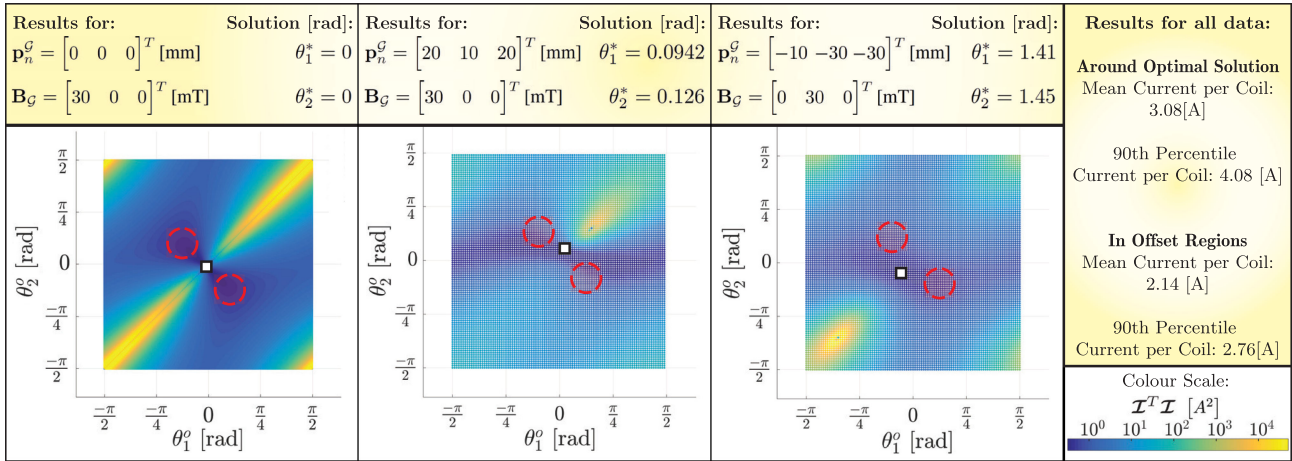


Fig. 4. Effect of coil fixture positions on the BigMag coil currents are studied for a total of 485 evenly distributed points (\mathbf{p}_n^G) within the workspace of BigMag, for different values of magnetic field (\mathbf{B}_G). The positions of coil fixtures have no significant impact on fields generated in vertical direction. For other investigated \mathbf{B}_G , the underdetermined system (15) is solved for coil currents (\mathcal{I}) for different fixture positions. These positions are located at an offset ($\theta_1^o, \theta_2^o \in [-\pi/2, \pi/2]$) from the solution provided by (19). Representative results are shown above. For all \mathbf{p}_n^G , the optimal coil fixture positions ($\theta^* = [\theta_1^* \ \theta_2^*]^T$) (white square) are found close (standard deviation 0.237 rad) to the solution proposed in (19). However, during the catheter steering, the actual fixture angles are used to compute \mathcal{I} . Those angles are likely to differ from optimal θ^* , provided as reference setpoint. Thus, we propose the use of solution (20), within the offset regions ($\theta_1^o, \theta_2^o \in [\pi/8, \pi/4]$) (red circles), yielding on average a much better current per coil performance.

the position of coil fixture ($\theta_f \in \mathcal{S}$), where $f \in \{1, 2\}$. The displacement vector ($\mathbf{r}_G^{C_k} \in \mathbb{R}^3$) describes the distance between origins of frames ($\{\mathcal{G}\}$ and $\{C_k\}$). The position of point (\mathbf{p}_n) in frame ($\{\mathcal{G}\}$) is described by $\mathbf{p}_n^G \in \mathbb{R}^3$. Noting that $\mathbf{p}_n^{C_k} = \mathbf{R}_G^{C_k} \mathbf{p}_n^G + \mathbf{r}_G^{C_k}$, the unit field map ($\beta_k^G(\mathbf{p}_n^G, \theta_f)$) of each coil (k), is represented as follows:

$$\beta_k^G(\mathbf{p}_n^G, \theta_f) = \mathcal{G}_{C_k} \mathbf{R}(\theta_f) \beta_{C_k}^{C_k}(\mathbf{p}_n^{C_k}) \quad (10)$$

$$\mathcal{G}_{C_k} \mathbf{R}(\theta_f) = \mathcal{G} \mathbf{R}(\theta_f) \mathcal{G}_{C_k}^T \mathbf{R}^0 \quad (11)$$

where $\mathcal{G} \mathbf{R}(\theta_f) \in \text{SO}(3)$ is the rotation matrix around Z -axis of frame ($\{\mathcal{G}\}$) (see Fig. 3) by an angle (θ_f) and $\mathcal{G}_{C_k} \mathbf{R}^0 \in \text{SO}(3)$ is the arbitrary reference configuration of coil (k).

The design of BigMag allows for direct control over the currents (\mathcal{I}) in each coil and position of coil fixtures ($\theta = [\theta_1 \ \theta_2]^T$). These variables are arranged into the input vector ($\eta = [\mathcal{I}^T \ \theta^T]^T \in \mathbb{R}^8$). The total magnetic field as a function of input (η) can be calculated using the forward map ($\gamma(\mathbf{p}_n^G, \eta)$)

$$\mathbf{B}_G = \gamma(\mathbf{p}_n^G, \eta) = \beta(\mathbf{p}_n^G, \theta) \mathcal{I} \quad (12)$$

$$\beta(\mathbf{p}_n^G, \theta) = [\beta_1^G(\mathbf{p}_n^G, \theta_1) \cdots \beta_3^G(\mathbf{p}_n^G, \theta_2) \cdots]. \quad (13)$$

The actuation of magnetic catheter requires solving a converse problem, which takes the form of an inverse field map ($\gamma^{-1}(\mathbf{B}_G, \mathbf{p}_n^G) = \eta$), allowing for generation of arbitrarily prescribed magnetic fields inside the workspace of BigMag. These fields are related to torques deflecting the catheter by (3).

B. Inverse Map of BigMag Coil Array

The most complete way of finding $\gamma^{-1}(\mathbf{B}_G, \mathbf{p}_n^G)$ would involve analytical inversion of (12), this task is challenging due to the nonlinearity of the forward map. Moreover, since the system

is overactuated, multiple solutions to inverse map arise. Alternatively, the computation of the inverse map can be formulated as the following optimization problem:

$$\min_{\mathcal{I}} \mathcal{I}^T \mathcal{I} \quad (14)$$

$$\text{s.t. } \mathbf{B}_G - \beta(\mathbf{p}_n^G, \theta) \mathcal{I} = 0 \quad (15)$$

minimizing the power consumption of the array for given \mathbf{B}_G . We note that for arbitrarily selected coil fixture positions (θ), the constraint in (15) can be solved using the damped pseudoinverse as follows:

$$\mathcal{I} = \beta^\dagger \mathbf{B}_G \quad (16)$$

$$\beta^\dagger = \beta^T (\beta \beta^T + \kappa^2 \mathbf{I}_6)^{-1} \in \mathbb{R}^{6 \times 3}. \quad (17)$$

The damping coefficient ($\kappa \in \mathbb{R}^+$, $\kappa \ll 1$.) is used to improve the behavior of the solution (\mathcal{I}), if β becomes ill-conditioned [26].

The optimization problem given by (14) and (15) can be reduced by means of eliminating the constraint (15) with the help of the solution (16) and (17). Consequently, an equivalent form of (14) is obtained as follows:

$$\min_{\mathcal{I}} (\mathcal{I}^T \mathcal{I}) \equiv \min_{\theta} (\mathbf{B}_G^T \beta^\dagger(\mathbf{p}_n^G, \theta)^T \beta^\dagger(\mathbf{p}_n^G, \theta) \mathbf{B}_G) \quad (18)$$

which involves evaluating the fixture positions (θ) for a given reference field (\mathbf{B}_G) and tip position (\mathbf{p}_n^G). Such a constraint elimination approach is valid due to the fact that the underdetermined system (15) has infinitely many solutions.

Nevertheless, solving (18) in real-time for catheter steering is challenging due to computational constraints. Thus, we propose a computationally fast approximate solution to (18). This solution is informed by a set of simulations (see Fig. 4), in which the cost function of the equivalent optimization problem

(18) is computed for \mathbf{B}_G at 485 points (\mathbf{p}_n^G) distributed evenly across the workspace (Ω_w). As follows from Fig. 4, the center of the workspace ($\mathbf{p}_n^G = \mathbf{0}_{3 \times 1}$), the current minimizing coil fixture positions ($\theta^* = [\theta_1^* \theta_2^*]^T \in \mathbb{S}^2$) are given by

$$\theta_1^* = \theta_2^* = (\text{atan2}(B_y^G, B_x^G) + n\pi) \quad (19)$$

where B_x^G and B_y^G are X and Y components of \mathbf{B}_G , respectively. Further, we notice that the optimal solutions for fields generated at other locations \mathbf{p}_n^G lie sufficiently close to (19) (standard deviation 0.237 rad), such that (19) can be considered an approximate solution of (18).

The approximate solution given by (19) has certain drawbacks for catheter steering. Since the mechanical bandwidth of the catheter is high, the prescribed (controlled) field (\mathbf{B}_G) should be generated quickly for a stable closed-loop system. However, steering the coil fixtures using (19) limits a fast response for \mathbf{B}_G due to the constraint on the velocity of the fixtures. Furthermore, if the difference between the present fixture angle and (19) is high, the actual field at the intermediate angles can vary significantly. This issue can be solved by using the actual angles instead of (19) and recomputing (16) in the intermediate fixture positions. At the same time, (19) is provided as a reference setpoint for the servo system driving the fixtures.

A further improvement to the issues with (19) can be obtained by introducing the following offsets:

$$\theta^* = (\text{atan2}(B_y^G, B_x^G) + n\pi) [1 \ 1]^T \pm [\theta_1^o \ -\theta_2^o]^T \quad (20)$$

to the approximate solution (θ^*). Here, the angle (θ_\star^o), for $\star = \{1, 2\}$ satisfies ($\theta_\star^o \in [\pi/8, \pi/4]$). In Fig. 4, it is shown that (20) provides a better field response compared to (19).

IV. VISION-BASED CATHETER SHAPE SENSING

Another crucial technology for the successful control of magnetic catheters is shape sensing. As follows from (3), both the position (\mathbf{p}_n) of the tip dipole as well as its magnetic dipole moment ($\boldsymbol{\mu}$) must be known to actuate the tip with a prescribed virtual wrench. Moreover, since the research problem presented in this paper involves the steering of the magnetic tip, its position (\mathbf{p}_n) is also required as a feedback to close the control loop. Finally, since the PRB approximation is used to derive the manipulator Jacobian, the PRBM configuration of the catheter (\mathbf{q}) must also be tracked and reconstructed in real-time.

In this section, we approach those challenges by using a point cloud processing technique for shape feedback. The entire approach is modular: the model recovery technique can be applied to point clouds from different sources, including medical imaging modalities, such as fluoroscopy or 3-D ultrasound. Consequently, we demonstrate how the variables needed for actuation and control of the catheter can be retrieved from the estimated shape ($\tilde{\mathbf{P}}(s)$).

The task of the catheter reconstruction (see Fig. 5) involves processing of a point cloud of size ($m \in \mathbb{Z}^+$), defined as a set

$$\mathbb{V}_t^0 = \{\mathbf{v}_i^0 \in \Omega_w\}, i = 1, \dots, m \quad (21)$$

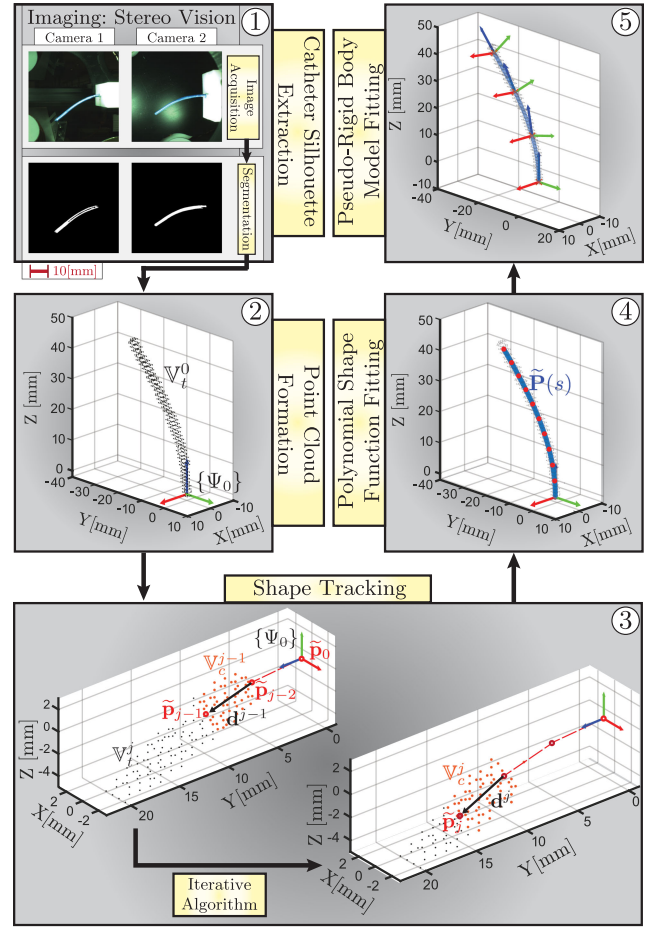


Fig. 5. Vision-based catheter tracking is a modular pipeline process, which can be divided into five major steps. ① The silhouette of the catheter is registered using stereo vision with two cameras. ② The point cloud (\mathbb{V}_t^0) with voxels describing catheter silhouette is formed for further processing. ③ An iterative algorithm computes a set of evenly spaced points ($\tilde{\mathbb{P}} = \{\tilde{\mathbf{p}}_j\}$) along the catheter shape. The fitting begins at the catheter origin ($\tilde{\mathbf{p}}_0$). In each iteration, the distance between $\tilde{\mathbf{p}}_{j-1}$ (established in previous iteration) and $\tilde{\mathbf{p}}_j$ is known. The subset ($\mathbb{V}_c^j \subset \mathbb{V}_t^j$) comprising of voxels within that distance is used to determine direction (\mathbf{d}^j) in which the $\tilde{\mathbf{p}}_j$ is located. Finally, $\tilde{\mathbf{p}}_j$ is calculated from 3-D line equation, and voxels in \mathbb{V}_c^j are excluded from further iterations. ④ The estimated catheter shape ($\tilde{\mathbf{P}}(s)$) is approximated by a polynomial function fitted onto $\tilde{\mathbb{P}}$. ⑤ This function is used for complete reconstruction of the PRBM used for closed-loop control. Note: all reference frames have red, green, and blue axes for X, Y, and Z, respectively.

where each voxel (\mathbf{v}_i^0) corresponds to a 3-D point contained within the silhouette of the device. The shape estimate ($\tilde{\mathbf{P}}(s)$) is recovered from \mathbb{V}_t^0 using iterative Algorithm 1. The procedure begins with finding the origin of the catheter ($\tilde{\mathbf{p}}_0$). The algorithm searches for all voxels within a close vicinity of the initial guess of the origin (\mathbf{p}_0^g), predefined by the user, and averages them to calculate $\tilde{\mathbf{p}}_0$ (see Algorithm 1, Lines 1–2). In our procedure, the user makes the initial guess for the first frame. Consequently, $\tilde{\mathbf{p}}_0$ for the previous point cloud is used as a guess for the current one.

Once the location of catheter origin is established, an iterative fitting procedure extracts a set ($\tilde{\mathbb{P}} = \{\tilde{\mathbf{p}}_j\}, j = 1, \dots, \tilde{n}$) of

Algorithm 1: Shape Reconstruction Algorithm.

Inputs:
 $\mathbb{V}_t^0 = \{\mathbf{v}_i\}$ \triangleright Set of voxels ($\mathbf{v}_i \in \mathbb{R}^3$)
 $\tilde{n} \in \mathbb{Z}$ \triangleright Number of points along catheter length to be found
 $l \in \mathbb{R}^+$ \triangleright Length of the manipulator
 \mathbf{p}_0^g \triangleright Initial guess for manipulator origin

Output:
 $\tilde{\mathbf{P}}(s)$ \triangleright Estimated shape function

Initialization:
1 *find all voxels* ($\mathbf{v}_o^0 \in \mathbb{V}_t^0 \mid \|\mathbf{v}_o^0 - \mathbf{p}_0^g\| \leq k_o$),
 $k_o \in \mathbb{R}^+$ is a constant distance
2 *take a mean over all* \mathbf{v}_o^0 *to find origin estimate* ($\tilde{\mathbf{p}}_0$)
for $j := 1$ **to** \tilde{n} **do** \triangleright Recursive Shape Fitting
3 $\mathbb{V}_c^j \leftarrow \{\mathbf{v}_i \in \mathbb{V}_t^{j-1} \mid \|\mathbf{v}_i - \tilde{\mathbf{p}}_{j-1}\| \leq \frac{l}{\tilde{n}}\}$
 \triangleright Find all voxels within distance ($\frac{l}{\tilde{n}}$) from $\tilde{\mathbf{p}}_{j-1}$
4 $\mathbf{d}^j \leftarrow \left[\begin{array}{c} \|\mathbf{v}_1^j - \tilde{\mathbf{p}}_{j-1}\| \mathbf{I}_3 \\ \vdots \\ \|\mathbf{v}_m^j - \tilde{\mathbf{p}}_{j-1}\| \mathbf{I}_3 \end{array} \right]^\dagger \left[\begin{array}{c} \mathbf{v}_1^j - \tilde{\mathbf{p}}_{j-1} \\ \vdots \\ \mathbf{v}_m^j - \tilde{\mathbf{p}}_{j-1} \end{array} \right]$
 \triangleright Use Moore-Penrose pseudoinverse (\dagger) to fit a line with direction (\mathbf{d}^j) to the voxel set (\mathbb{V}_c^j).
5 $\tilde{\mathbf{p}}_j \leftarrow \tilde{\mathbf{p}}_{j-1} + \frac{l}{\tilde{n}} N(\mathbf{d}^j)$
 \triangleright Find $\tilde{\mathbf{p}}_j$ using the normalised direction ($N(\mathbf{d}^j)$)
6 $\mathbb{V}_t^j \leftarrow \mathbb{V}_t^{j-1} \setminus \mathbb{V}_c^j$
 \triangleright Remove the voxels used for current iteration
end
7 $\tilde{\mathbf{P}}(s) := \mathbf{c}_\zeta s^\zeta + \dots + \mathbf{c}_1 s + \tilde{\mathbf{p}}_0$
 \triangleright Approximate $\tilde{\mathbf{P}}(s)$ with a polynomial function of chosen order ($\zeta \in \mathbb{Z}^+$), where $\mathbf{c}_* \in \mathbb{R}^3$ are the polynomial coefficients for $*$ = 1, ..., ζ
8 $\begin{bmatrix} \mathbf{c}_\zeta \\ \vdots \\ \mathbf{c}_1 \end{bmatrix} \leftarrow \begin{bmatrix} s_1^\zeta \mathbf{I}_3 & \dots & s_1 \mathbf{I}_3 \\ \vdots & \ddots & \vdots \\ s_n^\zeta \mathbf{I}_3 & \dots & s_n \mathbf{I}_3 \end{bmatrix}^\dagger \begin{bmatrix} \tilde{\mathbf{p}}_1 - \tilde{\mathbf{p}}_0 \\ \vdots \\ \tilde{\mathbf{p}}_n - \tilde{\mathbf{p}}_0 \end{bmatrix}$
 \triangleright find \mathbf{c}_* using pseudoinverse

points along $\tilde{\mathbf{P}}(s)$. The distance between each $\tilde{\mathbf{p}}_j$ and $\tilde{\mathbf{p}}_{j+1}$ is fixed to $\frac{l}{\tilde{n}}$. $\tilde{\mathbf{p}}_j$ is found in a series of steps. First, the set (\mathbb{V}_c^j) of all the voxels closer to $\tilde{\mathbf{p}}_{j-1}$ than $\frac{l}{\tilde{n}}$ is established (see Algorithm 1, Line 3). The number (\tilde{n}) is selected large enough, such that the shape of the catheter between $\tilde{\mathbf{p}}_{j-1}$ and $\tilde{\mathbf{p}}_j$ can be approximated with a straight line. The least-squares technique is used to find the direction $\hat{\mathbf{d}}$ of that line in 3-D space (see Algorithm 1, Line 4; Fig. 6). Since the desired distance to the next point is known, line equation is used to find $\tilde{\mathbf{p}}_j$ (see Algorithm 1, Line 6). Used voxels are excluded and the procedure repeats until the entire $\tilde{\mathbf{P}}$ is found.

Since the location of each element of $\tilde{\mathbf{P}}$ along $\tilde{\mathbf{P}}(s)$ is known, these points are used to fit the final shape function. We approximate the catheter shape with a parametric 3-D polynomial (see Algorithm 1, Line 7). The 3-D polynomials offer accurate shape representation combined with computational efficiency. The coefficients of the polynomial are found solving another least squares problem (see Algorithm 1, Line 8). Final shape of the device formed in this way (see Fig. 6) is used to calculate those parameters of the catheter, which are needed for closed-loop control.

Given the estimated shape function $\tilde{\mathbf{P}}(s)$, the PRBM is constructed as shown in Section II. Frame ($\{\Psi_s^0\}$) is positioned at the location of estimated catheter origin. For every 2-DoF PRBM joint (i), the parameters (q_i^x), (q_i^y) are found as follows:

$$q_i^x = -\text{atan2}(i^{-1}y_i, i^{-1}z_i), \quad q_i^y = \text{atan2}(i^{-1}x_i, i^{-1}z_i) \quad (22)$$

where

$$\begin{bmatrix} i^{-1}x_i & i^{-1}y_i & i^{-1}z_i & 1 \end{bmatrix}^T = {}^0_{i-1}\mathbf{H} \begin{bmatrix} \mathbf{p}_i^T & 1 \end{bmatrix}^T. \quad (23)$$

The transformation matrix (${}^0_{i-1}\mathbf{H} \in \text{SE}(3)$) is calculated using (6). The orientation of the magnetic tip, required for magnetic dipole moment estimation (and thus magnetic actuation), is computed using the normalized derivative of the shape function at the tip. The magnitude of the dipole ($\mu \in \mathbb{R}^+$) is assumed to be known beforehand. Hence, the total estimated tip dipole ($\boldsymbol{\mu}_{\text{est}} \in \mathbb{R}^3$) becomes

$$\boldsymbol{\mu}_{\text{est}} = \mu N \left(\left. \frac{d\mathbf{P}(s)}{ds} \right|_{s=l} \right) \quad (24)$$

where $N(\boldsymbol{\alpha}) = \frac{\boldsymbol{\alpha}}{\|\boldsymbol{\alpha}\|}$ for any vector ($\boldsymbol{\alpha}$).

V. CLOSED-LOOP STEERING OF MAGNETIC CATHETERS

In this section, we propose a technique for closed-loop steering of magnetic catheters. The PRBM of a catheter introduced in Section II is used to derive a nonlinear inverse model controller. The controller is used in conjunction with feedback from visual tracking and reconstruction presented in Section IV for real-time steering of magnetic catheter.

A. Inverse Model Control

In the proposed steering technique, the catheter is actuated by an external magnetic torque ($\boldsymbol{\tau}_\mu$), changing its shape dynamically until it reaches a static equilibrium approximated by the PRBM configuration (8). Since the dynamic behavior of the catheter moving towards the equilibrium exceeds the bandwidth of the available steering system, we disregard it. Therefore, we treat the static model (8) as a reduced-order model of the catheter, which can be used for controller design.

We begin the derivation of the controller reformulating the model (8). Since the gravity is represented by a single force acting on the catheter tip, it is useful to combine it with \mathbf{W} into a single wrench describing the total external load on the catheter. However, a problem arises, since gravitational force vector (\mathbf{F}_g) becomes dependent on the manipulator configuration (\mathbf{q}), if expressed in body frame of reference ($\{\Psi_s^n\}$). In spite of that, if we transform the body manipulator Jacobian ($\mathbf{J}_b(\mathbf{q})$), such that

$$\mathbf{J}_a(\mathbf{q}) = \begin{bmatrix} \mathbf{R}_n(\mathbf{q}) & \mathbf{0}_{3 \times 3} \\ \mathbf{0}_{3 \times 3} & \mathbf{I}_3 \end{bmatrix} \mathbf{J}_b(\mathbf{q}) \quad (25)$$

the total tip wrench (\mathbf{W}_t) can be defined as independent of the manipulator configuration. Hence, the following reformulation of (8) holds:

$$\mathbf{J}_a^T(\mathbf{q}) \mathbf{W}_t = \mathbf{C} \mathbf{q} \quad (26)$$

$$\mathbf{W}_t = \begin{bmatrix} \mathbf{F}_g \\ \boldsymbol{\tau}_\mu \end{bmatrix} = [\mathbf{0}_{1 \times 2} \quad -F_g \quad \tau_\mu^x \quad \tau_\mu^y \quad 0]^T. \quad (27)$$

Differentiation of (26) establishes the following relation between the rate of change of wrench elements ($\dot{\mathbf{W}}_t =$

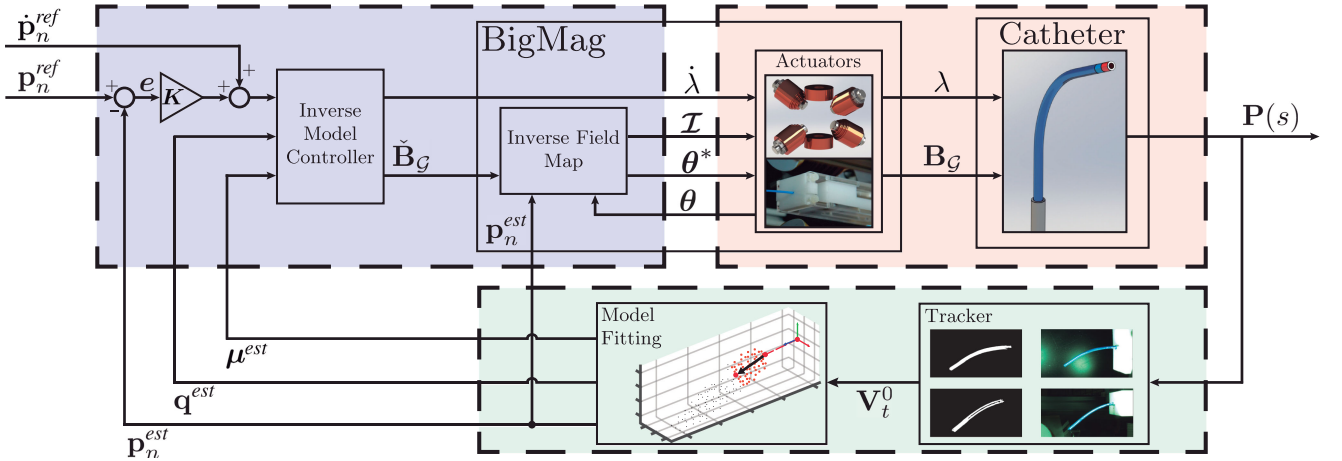


Fig. 6. Block diagram summarizing the system for closed-loop steering of magnetic catheters. An inverse model control (blue) is used to track a preprogrammed trajectory ($\mathbf{p}_n^{\text{ref}}$) of the tip of magnetic catheter using an inverse model control based on PRBM of the catheter. The controller provides reference magnetic field ($\tilde{\mathbf{B}}_G$) and catheter insertion velocity ($\dot{\lambda}$), which minimize the steering error (e). $\dot{\lambda}$ is a control variable fed directly to the automated catheter inserter. In the same time, $\tilde{\mathbf{B}}_G$ is generated using BigMag, using the technique presented in Section III to provide the rest of control variables: coil currents (\mathcal{I}) and reference fixture positions (θ), generating actual magnetic field (\mathbf{B}_G). This field determines the shape of the catheter ($\mathbf{P}(s)$). The shape-sensing (green) is provided for feedback in form of estimated tip position ($\mathbf{p}_n^{\text{est}}$), tip magnet dipole value ($\boldsymbol{\mu}^{\text{est}}$), and pseudorigid-body configuration (\mathbf{q}^{est}). These variables are recovered from a point cloud (\mathbf{V}_t^0) containing the silhouette of the catheter segmented from a tracker based on stereo vision.

$[\mathbf{0}_{1 \times 3} \quad \dot{\boldsymbol{\tau}}_\mu^T]^T$) and the PRBM joint rate ($\dot{\mathbf{q}}$):

$$\mathbf{C}\dot{\mathbf{q}} = \dot{\mathbf{J}}_a(\mathbf{q})^T \mathbf{W}_t + \mathbf{J}_a(\mathbf{q})^T \dot{\mathbf{W}}_t. \quad (28)$$

Using the chain rule, the product of \mathbf{W}_t and the rate of the Jacobian transpose ($\dot{\mathbf{J}}_a(\mathbf{q})^T$) is represented in a form, which is linear in $\dot{\mathbf{q}}$

$$\mathbf{C}\dot{\mathbf{q}} = \boldsymbol{\Gamma}(\mathbf{q}, \boldsymbol{\tau}_\mu)\dot{\mathbf{q}} + \mathbf{J}_a(\mathbf{q})^T \dot{\mathbf{W}}_t \quad (29)$$

where

$$\boldsymbol{\Gamma}(\mathbf{q}, \boldsymbol{\tau}_\mu) = \begin{bmatrix} -\frac{\partial J_a^{3,1}}{\partial \mathbf{q}} F_g + \frac{\partial J_a^{4,1}}{\partial \mathbf{q}} \tau_x^\mu + \frac{\partial J_a^{5,1}}{\partial \mathbf{q}} \tau_y^\mu & & \\ & \dots & \\ -\frac{\partial J_a^{3,2n}}{\partial \mathbf{q}} F_g + \frac{\partial J_a^{4,2n}}{\partial \mathbf{q}} \tau_x^\mu + \frac{\partial J_a^{5,2n}}{\partial \mathbf{q}} \tau_y^\mu & & \end{bmatrix}. \quad (30)$$

Hence, the final equation for PRBM joint rate becomes

$$\dot{\mathbf{q}} = (\mathbf{C} - \boldsymbol{\Gamma}(\mathbf{q}, \boldsymbol{\tau}_\mu))^{-1} \mathbf{J}_a^T(\mathbf{q}) [\mathbf{0}_{1 \times 3} \quad \dot{\boldsymbol{\tau}}_\mu^T]^T. \quad (31)$$

Differential equation (31) is used to design a MIMO inverse model controller to control the spatial position of the catheter tip (\mathbf{p}_n). If the transformed body Jacobian ($\mathbf{J}_a(\mathbf{q})$) is decomposed into linear ($\mathbf{J}_{a,v} \in \mathbb{R}^{3 \times 2n}$) and angular ($\mathbf{J}_{a,\omega} \in \mathbb{R}^{3 \times 2n}$) parts, such that $\mathbf{J}_a(\mathbf{q}) = [\mathbf{J}_{a,v}^T(\mathbf{q}) \quad \mathbf{J}_{a,\omega}^T(\mathbf{q})]^T$, the following holds:

$$\dot{\mathbf{p}}_n = \mathbf{J}_{a,v}(\mathbf{q})\dot{\mathbf{q}}. \quad (32)$$

Therefore, the relation between spatial tip velocity ($\dot{\mathbf{p}}_n$) and the rate of magnetic torque ($\dot{\boldsymbol{\tau}}_\mu$) is as follows:

$$\dot{\mathbf{p}}_n = \underbrace{\mathbf{J}_{a,v}(\mathbf{q}) (\mathbf{C} - \boldsymbol{\Gamma}(\mathbf{q}, \boldsymbol{\tau}_\mu))^{-1} \mathbf{J}_{a,\omega}^T(\mathbf{q})}_{\mathbf{A}(\mathbf{q}, \boldsymbol{\tau}_\mu)} \dot{\boldsymbol{\tau}}_\mu. \quad (33)$$

No torque can be generated in the direction parallel to the magnetic dipole ($\boldsymbol{\mu}$), as follows from (3) and (27). Thus, only 2 DoF can be controlled using the system described by (33), using torques (τ_μ^x) and (τ_μ^y). We mitigate that problem by including in the system an automated insertion device, which applies a linear displacement ($\lambda \in \mathbb{R}$) along the catheter insertion axis ($\hat{\lambda}$), as depicted in Fig. 2. Since this displacement can be controlled directly, we create the final actuation matrix ($\mathbf{A}_s(\mathbf{q}, \boldsymbol{\tau}_\mu) \in \mathbb{R}^{3 \times 3}$) used for steering as follows:

$$\mathbf{A}(\mathbf{q}, \boldsymbol{\tau}_\mu)\dot{\boldsymbol{\tau}}_\mu + \hat{\boldsymbol{\lambda}}\dot{\lambda} = \mathbf{A}_s(\mathbf{q}, \boldsymbol{\tau}_\mu) \begin{bmatrix} \dot{\tau}_\mu^x & \dot{\tau}_\mu^y & \dot{\lambda} \end{bmatrix}^T. \quad (34)$$

Using the matrix ($\mathbf{A}_s(\mathbf{q}, \boldsymbol{\tau}_\mu)$), the inverse-model controller can be formulated. We define the position error vector ($\mathbf{e} \in \mathbb{R}^3$), such that

$$\mathbf{e} = \mathbf{p}_n^{\text{ref}} - \mathbf{p}_n^{\text{est}} \quad (35)$$

where $\mathbf{p}_n^{\text{ref}} \in \mathbb{R}^3$ is the reference tip position and $\mathbf{p}_n^{\text{est}} \in \mathbb{R}^3$ is the current position estimate coming from the shape sensing technique described in Section IV. Using the quasi-static approach, the control equation takes the form

$$\mathbf{A}_s(\mathbf{q})^{-1}(\dot{\mathbf{p}}_n^{\text{ref}} + \mathbf{K}\mathbf{e}) = \begin{bmatrix} \dot{\tau}_\mu^x & \dot{\tau}_\mu^y & \dot{\lambda} \end{bmatrix}^T \quad (36)$$

where $\mathbf{K} \in \mathbb{R}^{3 \times 3}$ is a diagonal, positive-definite gain matrix, and $\dot{\mathbf{p}}_n^{\text{ref}}$ is the feed-forwarded reference tip velocity. The magnetic control torques are computed by numerically integrating the expressions ($\dot{\tau}_\mu^x$ and $\dot{\tau}_\mu^y$) given in (36). The corresponding reference magnetic field ($\tilde{\mathbf{B}}_G \in \mathbb{R}^3$) is consequently calculated using the following inverse map:

$$\tilde{\mathbf{B}}_G = \|\boldsymbol{\mu}_{\text{est}}\|^{-2} S(\boldsymbol{\mu}_{\text{est}}) \mathbf{R}_n(\mathbf{q}) \boldsymbol{\tau}_\mu. \quad (37)$$

In our study, $\tilde{\mathbf{B}}_G$ is generated by an array of mobile electromagnetic coils using the technique presented in Section III.

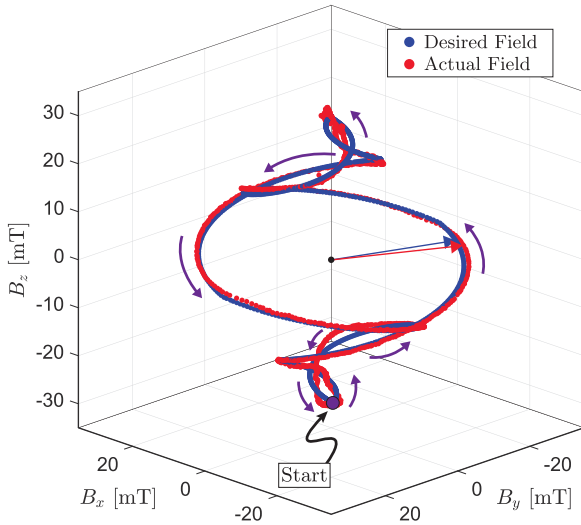


Fig. 7. Inverse magnetic field map presented in Section III is validated by using it to generate desired magnetic field trajectories in three locations within the workspace of BigMag. The figure shows the values of the desired field vector (blue arrow) and the measured one (red arrow) for 1500 samples along the trajectory generated at a point ($\mathbf{p}_n^G = [28.9 \ 28.9 \ 28.9]^T$ mm). The total percentage field magnitude error along all points from each trajectory is 2.20% and the mean angle between field vectors is 2.82° .

VI. EXPERIMENTAL VALIDATION

The control system (see Fig. 6) comprising of elements proposed in Sections II-V is implemented in C++14 on a computer running Linux Ubuntu 14.04.01, equipped with Intel Xeon E5 CPU, NVidia Quadro K4200 GPU, and 32 GB RAM. First, the inverse field map used for generation of control torques using BigMag is validated. Consequently, we test the shape sensing technique presented in Section IV. The shape sensing is implemented within BigMag to work with real-time point cloud data provided by a stereo vision system. Finally, a complete closed-loop steering framework is used to trace a series of 3-D trajectories within the workspace of BigMag.

A. Field Map Validation

The inverse map is validated by prescribing a set field trajectory (see Fig. 7) in three locations inside the workspace: at its centre ($\mathbf{p}^G = \mathbf{0}_{3 \times 1}$ mm) and at two remote locations ($\mathbf{p}^G = [30 \ 30 \ 0]^T$ mm) and ($\mathbf{p}^G = [28.9 \ 28.9 \ 28.9]^T$ mm). This trajectory is executed using the inverse map field technique presented in Section III. Senis 3MH3A-500MT (Senis AG, Baar, Switzerland) Teslometer is used to measure the actual field in a desired location. In total, 1500 samples are taken along each field trajectory. The sets of desired and actual field samples are compared showing an average error of 2.20%. The mean angle between the two field vectors is $2.82 \pm 1.15^\circ$, showing a significant improvement over our previous study [24].

B. Shape Sensing Validation

The shape sensing method, presented in Section IV, is implemented within BigMag system to process point cloud generated using the shape-from-silhouette approach [27]. The silhouette of

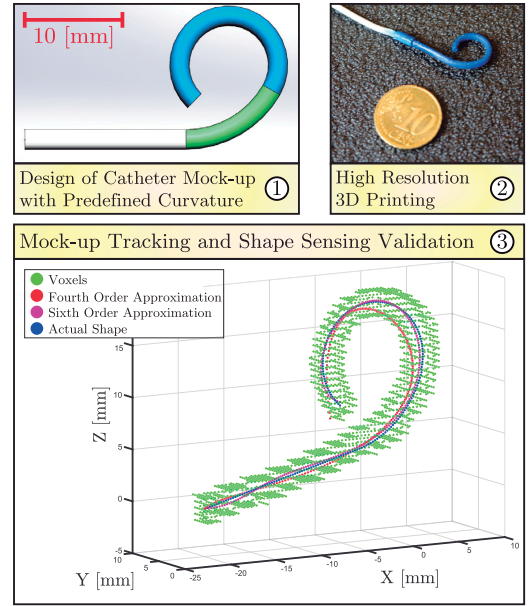


Fig. 8. Experimental procedure used to validate the shape sensing technique. ① A mock-up of a catheter with predefined shape is designed, and ② fabricated using 3-D printing technique. ③ The shape sensing technique proposed in this paper is used to retrieve polynomial shape estimate functions of different order. Those estimates are compared against known mock-up shape. The best results were observed for sixth order polynomial, with mean error of 0.59 mm.

the catheter is registered using stereo images coming from two Dalsa Genie Nano C1940 Red-Green-Blue cameras (Teledyne Dalsa, Waterloo, ON, Canada) (see Fig. 3). The side camera is equipped with Cinegon 1.6/16 (Schneider, Rueil-Malmaison, France) lens providing a depth of field of 120 mm with near limit of 111.2 mm. The top camera employs Cinegon 10/1.9 (Schneider, Rueil-Malmaison, France) lens, providing an infinite field depth with near limit of 52.1 mm. Both cameras are calibrated in a stereo configuration using Camera Calibration Toolbox (Mathworks, Natick, MA, USA). Segmented silhouettes are used to generate catheter point cloud using space carving technique. The resulting point cloud (\mathbb{V}_t^0) is fed into Algorithm 1 for shape sensing.

The validation of the shape sensing involves using the technique presented in Section IV on a catheter mock-up with predefined curvature (see Fig. 8). This mock-up is designed using CAD technique and fabricated on a high resolution 3-D printer. The known shape ($\mathbf{P}(s)$) for a set of points along the length of the mock-up is compared against the shape estimate function ($\tilde{\mathbf{P}}(s)$) using Algorithm 1 with three different polynomial orders ($\zeta = 4, 5, 6$). The error between $\mathbf{P}(s)$ and $\tilde{\mathbf{P}}$ was measured in a total of 200 locations (s). The average errors are 1.5 mm for $\zeta = 4$, 0.88 mm for $\zeta = 5$, and 0.59 mm for $\zeta = 6$.

C. Closed-Loop Steering

Ultimately, the system proposed in this paper is tested in final steering experiments. First, the implementation of the control framework has been benchmarked for computational performance. The average execution time of different software

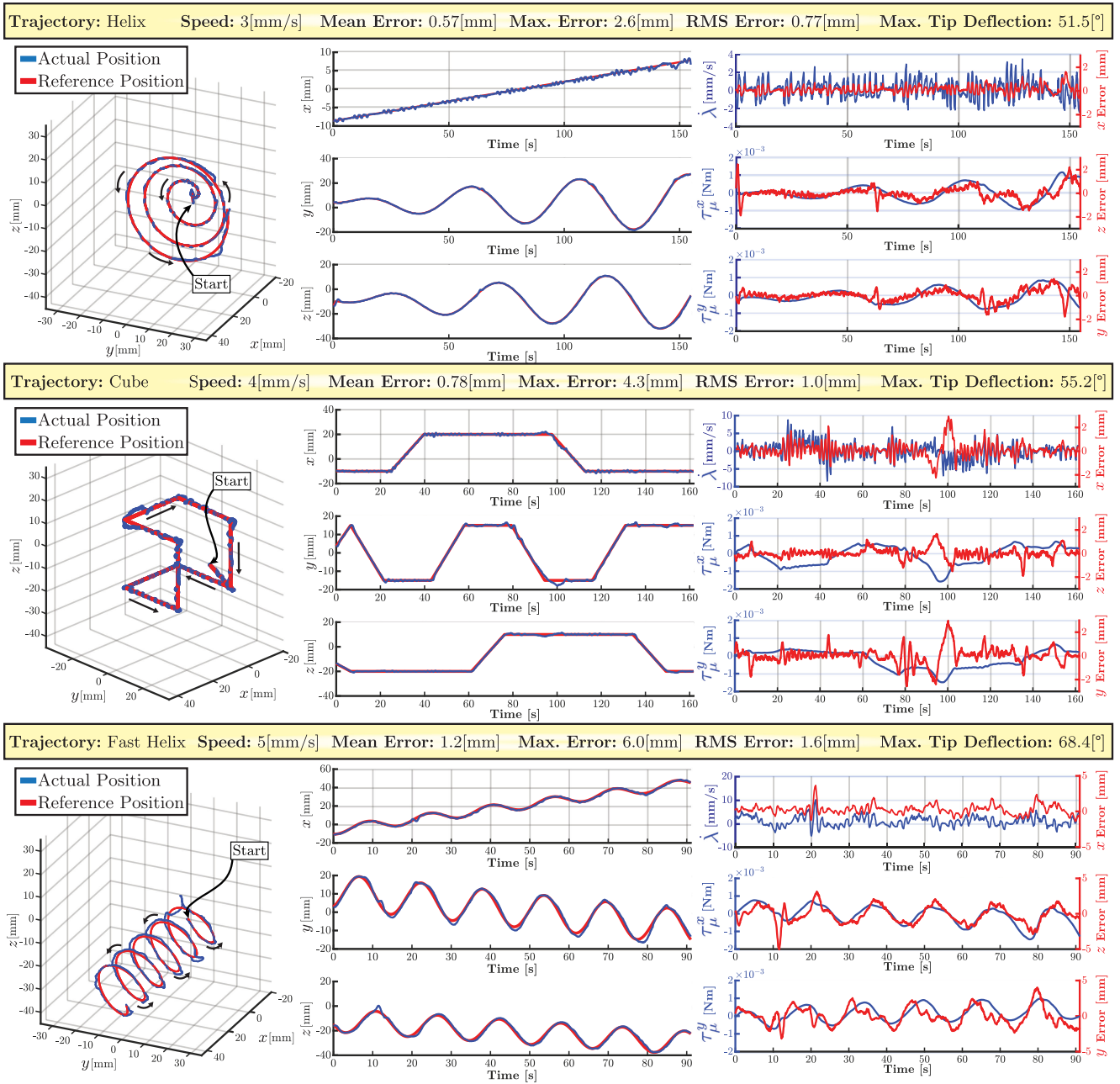


Fig. 9. Catheter is steered inside the workspace (Ω_w) of BigMag along three trajectories with various geometries and speeds. For each trajectory the mean, maximum, and RMS steering error is measured. Left: The spatial trajectory of catheter tip in Cartesian coordinates (x, y, z) of Ω_w . Centre: Time plot of reference and actual tip position for each spatial coordinate. Right: Time plot of error signal (e) spatial components, and outputs of control equation (36): magnetic torques (τ_{μ}^x) and (τ_{μ}^y), and catheter insertion velocity (λ).

components is as follows: BigMag field map (see Section III) — 350 μ s; inverse model controller (see Sections II and VI) — 1.8 ms; stereo image acquisition and processing — 35.2 ms, shape reconstruction (see Section IV) — 2.4 ms. The total computational time of software components allows for 25 Hz closed loop control. Nevertheless, to eradicate all possible jitter, predominantly due to variable image acquisition time (up to 60 ms), the actual control cycle is set to 10 Hz.

The controller is used to track three trajectories presented in Fig. 9, each with different speed. The results show that the proposed control framework can be used for position steering

of catheter tip with minimum recorded mean trajectory error of 0.57 mm (RMS error 0.77 mm). The maximum reached catheter speed was 5 mm/s. (Please refer to the video in supplementary material for demonstration of the experimental results.)

The steering errors can be explained by several phenomena observed during the experiments. First of all, the vision-based shape sensing method generates noise, mostly due to limitations of the catheter base detection scheme (see Algorithm 1, Lines 1–2). This noise can be observed in Fig. 9 as a fast-oscillating component of the error signal. Furthermore, the reduced order of the system due to quasi-static assumption caused further

performance deterioration at higher velocities, due to the uncompensated higher order dynamics of the catheter, as well as relatively low frequency of the control cycle. Moreover, at larger tip deflection, the PRB modeling approach becomes less accurate, degrading the performance of the controller. Finally, the effect of magnetic force (F_μ) resulted in larger steering error close to the edges of BigMag workspace, where magnetic field gradients are more prominent.

The maximum reported catheter position error of 6.0 mm does not guarantee reliable operation within smaller sections of human cardiovascular system. Even though high compliance of the device, as well as small magnitudes of control torques prevent significant tissue damage, the positioning precision should be improved. The decrease of the maximum error at lower velocities of the catheter indicates that increasing the bandwidth of the control system, or extending the controller to account for the dynamics of both the catheter and the coil system, could contribute to that.

Improving several other aspects of the presented framework can facilitate the translation of magnetic catheter steering into clinical practice. The current size of workspace offered by BigMag restricts the procedures to catheter positioning tasks within human limbs. Development of a system capable of running the presented framework at sufficient bandwidth in a clinically relevant workspace remains a relevant, ongoing technical challenge. Furthermore, the majority of clinical procedures require achieving successful, predictable contact between the catheter and the tissues of the body. This limits the applicability of the framework, as it does not include the presence of contact forces. Including these forces in the PRB model, and developing a reliable force sensing method could offer the possibility of realizing force control in a manner similar to [5].

VII. CONCLUSION AND FUTURE WORK

In this paper, a modular approach for closed-loop control of magnetic endovascular catheters is presented. The catheter is represented using pseudo-rigid-body modeling, taking into account the effects of magnetic and gravitational forces. Based on PRBM approach, a nonlinear, inverse-model position controller is derived for steering catheter using magnetic actuation. The magnetic field used for steering is generated by BigMag, an array of mobile electromagnets. A stereo-vision system is used to provide catheter shape information, as well as to track the catheter tip position to close the control loop.

The presented framework is tested experimentally. The inverse map technique used with BigMag to generate reference field is tested, showing an average error of 2.20%. The shape sensing technique is validated as capable of retrieving the shape of the catheter with a mean error of 0.59 mm. Finally, all the components of the system are integrated and the framework is evaluated in catheter steering experiments across a set of trajectories. The minimum reported mean position error is 0.57 mm (RMS error 0.77 mm), and the maximum catheter tip speed achieved is 5 mm/s.

In future studies, we want to focus on improving the control of the catheter, as well as on translating the presented technology

closer to clinical practice. We will extend the PRBM approach to account for manipulator dynamics, including during the contact phase with a soft tissue. This should alleviate the problems related to reduced order of the controller and allow for extending the framework to be applied during force control tasks. Moreover, we will employ faster shape sensing techniques, providing higher effective control frequency. Finally, we plan to do experiments in clinically relevant scenarios, using our framework with BigMag, as well as with new systems with improved workspaces to steer catheters in phantoms under the guidance of medical imaging modalities.

REFERENCES

- [1] J. M. Tobis and I. Abudayyeh, "New devices and technology in interventional cardiology," *J. Cardiol.*, vol. 65, no. 1, pp. 5–16, 2015.
- [2] A. Ali, D. H. Plettenburg, and P. Breedveld, "Steerable catheters in cardiology: Classifying steerability and assessing future challenges," *IEEE Trans. Biomed. Eng.*, vol. 63, no. 4, pp. 679–693, Apr. 2016.
- [3] C. Piorkowski *et al.*, "Steerable versus nonsteerable sheath technology in atrial fibrillation ablation: a prospective, randomized study," *Circulation: Arrhythmia Electrophysiol.*, vol. 4, no. 2, pp. 157–165, 2011.
- [4] G. J. Vrooijink, T. Ellenbroek, P. Breedveld, J. G. Grandjean, and S. Misra, "A preliminary study on using a robotically-actuated delivery sheath (RADS) for transapical aortic valve implantation," in *Proc. IEEE Int. Conf. Robot. Automat.*, Hong Kong, 2014, pp. 4380–4386.
- [5] A. Bajo and N. Simaan, "Hybrid motion/force control of multi-backbone continuum robots," *Int. J. Robot. Res.*, vol. 35, no. 4, pp. 422–434, 2016.
- [6] R. J. Webster and B. A. Jones, "Design and kinematic modeling of constant curvature continuum robots: A review," *Int. J. Robot. Res.*, vol. 29, no. 13, pp. 1661–1683, 2010.
- [7] T. Kimura *et al.*, "Operator-blinded contact force monitoring during pulmonary vein isolation using conventional and steerable sheaths," *Int. J. Cardiol.*, vol. 177, no. 3, pp. 970–976, 2014.
- [8] H. Tillander, "Magnetic guidance of a catheter with articulated steel tip," *Acta Radiologica*, vol. 35, no. 1, pp. 62–64, 1951.
- [9] C. Heunis, J. Sikorski, and S. Misra, "Flexible instruments for endovascular interventions: Improved magnetic steering, actuation, and image-guided surgical instruments," *IEEE Robot. Automat. Mag.*, vol. 25, no. 3, pp. 71–82, Sep. 2018.
- [10] F. Settecase *et al.*, "Magnetically-assisted remote control (MARC) steering of endovascular catheters for interventional MRI: A model for deflection and design implications," *Med. Phys.*, vol. 34, no. 8, pp. 3135–3142, 2007.
- [11] T. Liu, N. L. Poirot, D. Franson, N. Seiberlich, M. Griswold, and M. Cavusoglu, "Modeling and validation of the three dimensional deflection of an MRI-Compatible magnetically-actuated steerable catheter," *IEEE Trans. Biomed. Eng.*, vol. 63, no. 10, pp. 2142–2154, Oct. 2016.
- [12] M. P. Kummer, J. J. Abbott, B. E. Kratochvil, R. Borer, A. Sengul, and B. J. Nelson, "Octomag: An electromagnetic system for 5-DOF wireless micromanipulation," *IEEE Trans. Robot.*, vol. 26, no. 6, pp. 1006–1017, Dec. 2010.
- [13] V. N. T. Le, N. H. Nguyen, K. Alameh, R. Weerasooriya, and P. Pratten, "Accurate modeling and positioning of a magnetically controlled catheter tip," *Med. Phys.*, vol. 43, no. 2, pp. 650–663, 2016.
- [14] T. Greigarn and M. C. Çavuşoğlu, "Pseudo-rigid-body model and kinematic analysis of MRI-actuated catheters," in *Proc. IEEE Int. Conf. Robot. Automat.*, Seattle, WA, USA, 2015, pp. 2236–2243.
- [15] S. W. Hetts *et al.*, "Endovascular catheter for magnetic navigation under MR imaging guidance: Evaluation of safety in vivo at 1.5 T," *Amer. J. Neuroradiol.*, vol. 34, no. 11, pp. 2083–2091, 2013.
- [16] B. L. Nguyen, J. L. Merino, and E. S. Gang, "Remote navigation for ablation procedures—a new step forward in the treatment of cardiac arrhythmias," *Eur. Cardiol.*, vol. 6, no. 3, pp. 50–56, 2010.
- [17] F. Ullrich, S. Schuerle, R. Pieters, A. Dishy, S. Michels, and B. J. Nelson, "Automated capsulorhexis based on a hybrid magnetic-mechanical actuation System," in *Proc. IEEE Int. Conf. Robot. Automat.*, 2014, pp. 4387–4392.
- [18] K. J. Boskma, S. Scheggi, and S. Misra, "Closed-loop control of a magnetically-actuated catheter using two-dimensional ultrasound images," in *Proc. 6th IEEE RAS/EMBS Int. Conf. Biomed. Robot. Biomechanics*, Singapore, 2016, pp. 61–66.

- [19] S. L. Charreyron, B. Zeydan, and B. J. Nelson, "Shared control of a magnetic microcatheter for vitreoretinal targeted drug delivery," in *Proc. IEEE Int. Conf. Robot. Automat.*, Singapore, 2017, pp. 4843–4848.
- [20] J. Edelmann, A. J. Petruska, and B. J. Nelson, "Magnetic control of continuum devices," *Int. J. Robot. Res.*, vol. 36, no. 1, pp. 68–85, 2017.
- [21] D. B. Camarillo, K. E. Loewke, C. R. Carlson, and J. K. Salisbury, "Vision based 3-D shape sensing of flexible manipulators," in *Proc. IEEE Int. Conf. Robot. Automat.*, Pasadena, CA, USA, 2008, pp. 2940–2947.
- [22] J. M. Croom, D. C. Rucker, J. M. Romano, and R. J. Webster, "Visual sensing of continuum robot shape using self-organizing maps," in *Proc. IEEE Int. Conf. Robot. Automat.*, Anchorage, AK, USA, 2010, pp. 4591–4596.
- [23] R. J. Roesthuis and S. Misra, "Steering of multisegment continuum manipulators using rigid-link modeling and FBG-based shape sensing," *IEEE Trans. Robot.*, vol. 32, no. 2, pp. 372–382, Apr. 2016.
- [24] J. Sikorski, I. R. Dawson, A. Denasi, E. E. G. Hekman, and S. Misra, "Introducing—A novel system for 3D actuation of flexible surgical devices," in *Proc. IEEE Int. Conf. Robot. Automat.*, Singapore, 2017, pp. 3594–3599.
- [25] A. J. Petruska, J. Edelmann, and B. J. Nelson, "Model-based calibration for magnetic manipulation," *IEEE Trans. Magn.*, vol. 53, no. 7, Jul. 2017, Art. no. 4900206.
- [26] S. Chiaverini, B. Siciliano, and O. Egeland, "Review of the damped least-squares inverse kinematics with experiments on an industrial robot manipulator," *IEEE Trans. Control Syst. Technol.*, vol. 2, no. 2, pp. 123–134, Jun. 1994.
- [27] A. Laurentini, "The visual hull concept for silhouette-based image understanding," *IEEE Trans. Pattern Anal. Mach. Intell.*, vol. 16, no. 2, pp. 150–162, Feb. 1994.



Jakub Sikorski (S'17) received the M.Eng. degree in biomedical engineering from The University of Glasgow, Glasgow, U.K., in 2015. He is currently working toward the Doctoral degree with the Surgical Robotics Laboratory, University of Twente, Enschede, The Netherlands.

His work focuses on design, modelling, and control of magnetic catheters for minimally invasive surgical procedures. His research interests include continuum robotics, magnetic actuation, mechatronic design, and control of medical devices.



Alper Denasi (M'18) received the M.Sc. and Ph.D. degrees in mechanical engineering from the Eindhoven University of Technology, Eindhoven, The Netherlands, in 2009 and 2015, respectively.

Since 2015, he has been a Postdoctoral Fellow with the University of Twente, Enschede, The Netherlands. Since 2017, he has been a Postdoctoral Fellow with the University Medical Center, Groningen, The Netherlands. His current research interests include modeling, control and

identification/estimation of microrobotic systems, and flexible medical instruments such as continuum robots.



Giuseppe Bucchi received the B.Sc. degree in biomedical engineering in 2015 from the Politecnico di Milano, Milan, Italy, where he is currently working toward the M.Sc. degree in biomedical engineering.

In April 2017, he joined Surgical Robotics Laboratory, University of Twente, Enschede, The Netherlands, to work on the Master's degree focused on shape sensing and modeling of magnetic catheters.



Stefano Scheggi received the M.Sc. and Ph.D. degrees in computer engineering from the University of Siena, Siena, Italy, in 2007 and 2012, respectively.

In 2011, he was a Visiting Ph.D. Student with the Department of Computer Science, George Mason University, Fairfax, VA, USA, under the supervision of Prof. J. Kosecka. Since 2012, he has been a Postdoctoral Fellow with the University of Siena. Since 2015, he has been a Postdoctoral Fellow with the University of Twente,

Enschede, The Netherlands. His research interests include computer vision, medical robotics, haptics, and augmented/virtual reality.



Sarthak Misra (S'05–M'10) received the Master's degree in mechanical engineering from McGill University, Montréal, QC, Canada, in 2001, and the Doctoral degree in mechanical engineering from The Johns Hopkins University, Baltimore, MD, USA, in 2009.

He is currently a Professor within the Department of Biomechanical Engineering, University of Twente, Enschede, The Netherlands, and also affiliated with the Department of Biomedical Engineering, University of Groningen, The Netherlands,

and University Medical Center Groningen, The Netherlands. Prior to commencing his doctoral studies he was a Dynamics and Controls Analyst on the International Space Station Program. His research interests include surgical robotics and medical microrobotics.

Prof. Misra was the recipient of the European Research Council Starting and Proof-of-Concept Grants and the Netherlands Organization for Scientific Research VENI and VIDI Award. He is a Co-Chair of the Robotics and Automation Society Technical Committee on Surgical Robotics and a Co-Chair of the International Federation of Automatic Control Technical Committee on Biological and Medical Systems.